Noise-related polarization dynamics for femto and picosecond pulses in normal dispersion fibers

JAMES S. FEEHAN,[1,*] ORCID ENRICO BRUNETTI,[1] SAMUEL YOFFE,[1] WENTAO LI,[1] SAMUEL M. WIGGINS,[1] DINO A. JAROSZYNSKI,[1] AND JONATHAN H. V. PRICE[2] ORCID

[1] *Scottish Universities Physics Alliance, Department of Physics, University of Strathclyde, Glasgow G4 0NG, UK*
[2] *Optoelectronics Research Centre, University of Southampton, Hampshire SO17 1BJ, UK*
*james.feehan@strath.ac.uk

Abstract: We report how the complex intra-pulse polarization dynamics of coherent optical wavebreaking and incoherent Raman amplification processes in all-normal dispersion (ANDi) fibers vary for femto and picosecond pump pulses. Using high temporal resolution vector supercontinuum simulations, we identify deterministic polarization dynamics caused by wavebreaking and self-phase modulation for femtosecond pulses and quasi-chaotic polarization evolution driven by Raman amplification of quantum noise for picosecond pulses. In contrast to cross-phase modulation instability, the Raman-based polarization noise has no power threshold and is reduced by aligning the higher energy polarization component with the lower index axis of the fiber. The degree of polarization stability is quantified using new time domain parameters that build on the spectrally averaged degree of coherence used in supercontinuum research to quantify the output spectral stability. We show that the spectral coherence is intrinsically linked to polarization noise, and that the noise will occur in both polarization maintaining (PM) and non-PM fibers, spanning a broad range of pulse energies, durations, and fiber birefringence values. This analysis provides an in-depth understanding of the nonlinear polarization dynamics associated with coherent and incoherent propagation in ANDi fibers.

1. Introduction

Supercontinuum generation in all-normal dispersion (ANDi) photonic crystal fiber (PCF) offers an energy-scalable route to developing high brightness, single cycle sources with octave-spanning bandwidths [1–4]. Pumping in the ANDi regime relaxes constraints on the short pulse durations required to maintain excellent spectral coherence by an order of magnitude in comparison with anomalous dispersion pumping [5,6] by ensuring that pulse-preserving optical wavebreaking is the dominant spectral broadening process [7,8]. This increases the range of pump sources available for coherent supercontinuum generation and potentially reduces system cost and complexity. Applications include optical coherence tomography [9,10], frequency metrology [11] with possible extension to gigahertz repetition rates [12], coherent anti-Stokes Raman scattering [13], and mid-infrared photonics [14–16]. However, the applicability of these sources is limited when noise amplifying effects dominate the propagation and wavebreaking does not occur. Consequently, investigating the causes and complex dynamics of coherent pulse-preserving and incoherent noise amplifying effects in ANDi PCF is currently at the forefront of supercontinuum research [6,17–19]. In this paper, we extend recent research to consider the previously unexplored polarization dynamics of both coherent and incoherent ANDi supercontinuum generation.

For pulse durations above approximately 1.5 ps, non-phase-matched Raman-assisted parametric four-wave mixing (FWM) leads to the amplification of out-of-band quantum noise [6,20–22]. This degrades the pulse coherence starting from its leading edge when the influence of Raman amplification surpasses that of the coherent self phase modulation (SPM) and optical wavebreaking processes, i.e. when dispersion is high, or when a long fiber or pump pulse duration is used [6]. Additionally, a recent numerical investigation has shown that cross-phase modulation (XPM) can assist Raman-based decoherence of orthogonally polarized pulse components [19], which depends on the polarization group velocity mismatch (GVM). The output coherence of the low energy component is highest when it is polarized along the high index fiber axis because this minimizes its overlap with the incoherent leading edge of the high energy component. The effect is distinct from other birefringence-dependent effects [23], cross-phase and polarization modulation instability (MI), which also lead to decoherence and destabilization of the pulse polarization in ANDi supercontinuum generation [24–26] or, equivalently, with normal dispersion pumping in step-index silica fibers [27].

Here, we study the nonlinear polarization dynamics associated with both coherent and incoherent spectral broadening processes in ANDi PCF. We build on the concept of wavelength dependent coherence, commonly used in supercontinuum generation and frequency metrology, to define new measures of the intra-pulse polarization evolution in the time domain, which allow us to compare the spectral coherence with the polarization dynamics, as is required to study time domain applications of ultrafast pulses such as optical switching and gating.

We first confirm that the nonlinear polarization dynamics associated with coherent optical wavebreaking are deterministic. Then we identify two distinct polarization regimes for incoherently broadened pulses: a deterministic regime of quickly varying polarization where SPM and XPM contribute most strongly at the leading and trailing pulse edges, and a noise-dominated polarization regime that starts from the pulse leading edge then moves towards the peak when Raman-assisted parametric FWM and XPM dominate. We show that polarization noise occurs in both polarization maintaining (PM) and non-PM fibers, and is reduced (but not eliminated) when the GVM asymmetry of the XPM-assisted Raman amplification is exploited by aligning the highest energy polarization component to the low index fiber axis. Unlike cross-phase MI, Raman-based polarization noise has no power threshold.

We study pulse parameters typical of megahertz repetition rate sub-10 ps lasers operating around 1 μm (e.g., Yb fiber, Yb:KGW, Nd:glass) and a PCF design with a dispersion at this wavelength which approximates that of step-index silica fiber, ensuring that our findings are also applicable to other research areas. Similar polarization instabilities may also arise in systems with gain, such as picosecond fiber amplifier systems limited by Raman [28], fiber chirped pulse amplification systems limited by SPM and XPM [29], parabolic amplifiers [30], fiber-based optical parametric oscillators and amplifiers [31,32], nonlinear optical and amplifying loop mirrors [33,34], sources of noise-like pulses based on Raman amplification and nonlinear polarization evolution in ANDi fiber cavities [35,36], and telecommunications systems which combine Raman and FWM to extend transmission bandwidths beyond what is achievable in Er-doped fiber [37,38].

Our identification of deterministic and noise-dominated polarization regimes is potentially relevent to sources based on materials other than silica. For example, low loss gas filled hollow core fibers [39] are useful for spectroscopy and sub-femtosecond pulse generation in the vacuum ultraviolet [40,41], with research motivated by their tunable dispersion profiles [42]. The large Raman contribution of, for example, atmospheric gasses [43–45] suggests that with picosecond pumping Raman-induced polarization noise could occur even more readily in these sources [46]. Similarly, our observed polarization dynamics may occur in much shorter lengths of normal dispersion liquid core fiber than ANDi silica PCF [47,48] because of the larger nonlinear index of many liquids in comparison with silica [49], and because many gas and liquid core fibers

permit strong polarization mode coupling. Additionally, both deterministic and noise-dominated polarization dynamics are expected to occur in ANDi supercontinuum generation pumped by different pulsed sources, such as lasers used to seed chalcogenide or fluoride fiber for mid-infrared generation [15,50–52].

Section 2 introduces our model. In section 3 we show how optical wavebreaking and XPM affect the polarization dynamics of femtosecond pump pulses. In section 4 we show how the polarization stability of picosecond pump pulses is affected by Raman amplification, SPM, and XPM. In section 5 we show how the polarization stability is affected by the competition between wavebreaking and Raman amplification in both weakly and strongly birefringent fibers. In section 6 we outline key distinctions between cross-phase and polarization MI and the Raman-based polarization noise. Section 7 concludes the work.

2. Numerical model

We use a polarization-resolved vector extension of the generalized nonlinear Schrödinger equation (GNLSE) to simulate the pulse propagation (see Appendix A for equations and the integration methods). The GVM is adjusted over the range ±2 ps/m, corresponding to a maximum fiber birefringence of $\Delta n = 6 \times 10^{-4}$ and a minimum beat length of 1.7 mm. Hence we consider both PM and non-PM fibers [53].

The input pulses have a central wavelength of $\lambda_0 = 1040$ nm and a Gaussian temporal field profile given by $A(T) = \sqrt{P_0}\exp[-2\ln(2)(T/T_0)^2]$, where P_0 is the peak power, $T = t - z/v_{gx}$, z is the propagated distance, v_{gx} is the group velocity of the central wavelength of the x-polarized field component (denoted A_x throughout), and T_0 is the full width at half maximum (FWHM) pulse duration. This definition of T allows for the y polarization component to be advanced or delayed using the GVM, $\Delta\beta_1 = \beta_{1x} - \beta_{1y}$. Our aim is to investigate the influence of XPM, SPM, optical wavebreaking, and Raman amplification on the intra-pulse polarization and spectral coherence, so we assume transform limited pulses throughout. Strongly chirped pulses do not significantly modify the general characteristics of these effects (see Ref. [6]), so the coherence of, e.g., 100 fs pump pulses chirped to ~10 ps would evolve in a similar way to the coherence of the picosecond pump pulses shown here.
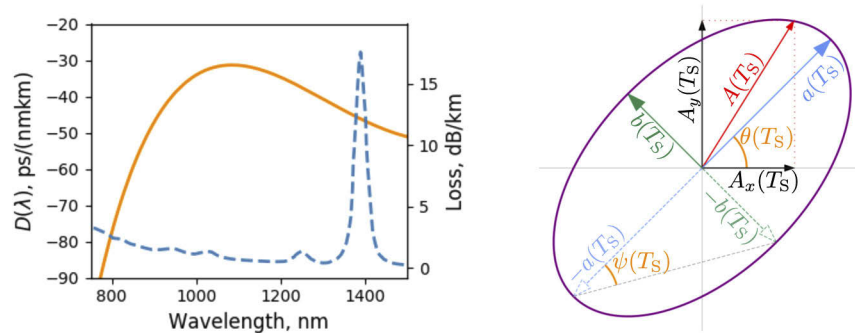

Fig. 1. Left, orange solid (left axis): Dispersion curve for the silica hexagonal lattice ANDi PCF. $\Lambda = 1.7$ μm, and $d/\Lambda = 0.3$. Left, blue dashed (right axis): Loss profile used in the simulations. Right: Visual representation of the orientation, θ (Eq. (5)), and ellipticity, ψ (Eq. (6)), at snapshot time T_S. A_x and A_y are the x- and y-polarized field envelopes, and a (Eq. (7)) and b (Eq. (8)) are the semi-major and semi-minor polarization axes, respectively.

The ANDi PCF dispersion (left plot, solid line in Fig. 1) and nonlinear response, $\gamma = 2\pi n_2/(\lambda A_{\text{eff}})$, are calculated using an analytical approach [54,55] with an air hole pitch and relative size of $\Lambda = 1.7$ μm and $d/\Lambda = 0.3$, respectively, where n_2 is the nonlinear index, λ

is wavelength, and A_{eff} is the effective mode area. (The wavelength dependence of γ is also included). For these parameters, $\gamma(\lambda_0) = 0.03$ rad/(Wm) and $D(\lambda_0) = -31$ ps/(nm km). Loss is equal to that of standard single mode silica fibers [56] (left plot, dashed line in Fig. 1), and the fiber length is 1 m for all of the simulations. The Raman effect is included using the experimentally measured silica response [57] via a fractional contribution to the nonlinear response of $f_R = 0.18$, and has a peak frequency detuning of $\Omega_R/(2\pi) = 13.2$ THz (47.6 nm at λ_0).

We use the soliton number (Eq. (1)) to interpret the results. The dispersion length is given by $L_D = T_0^2/|\beta_2|$, and $L_N = 1/(\gamma P_0)$ is the nonlinear length. Equations (2) give the characteristic lengths for coherent optical wavebreaking, L_{WB}, and incoherent Raman-assisted parametric FWM, $L_R^\star$ [6]. Here, $g_s^\star = 2\gamma\text{Re}\left(\sqrt{K(2q - K)}\right)$ is the mixed parametric-Raman gain coefficient [20–22], $K = -\beta_2\Omega_R^2/(2\gamma P_0)$ is the ratio of the linear and nonlinear contributions to the phase mismatch between the pulse and (anti-)Stokes wave, $q = (1 - f_R) - f_R\tilde{\chi}_R^{(3)}(-\Omega_R)$, and $\tilde{\chi}_R^{(3)}$ is the complex Raman susceptibility ($-1.38i$ at the Raman peak frequency detuning [22]). The ratio $L_R^\star/L_{\text{WB}}$ quantifies the competition between SPM/optical wavebreaking processes and Raman-assisted parametric FWM, and is central to determining whether the output will be coherent or incoherent [6].

$$N = \sqrt{\frac{L_D}{L_N}} \tag{1}$$

$$L_{\text{WB}} \approx 1.1\sqrt{L_D L_N}, \qquad L_R^\star = \frac{1}{g_s^\star P_0} \tag{2}$$

We study ensembles of 60 pulses, forming 1770 unique pairs (see Appendix B for numerical methods). Each pulse has different one photon per mode and per polarization axis quantum noise [5,24] and spontaneous Raman scattering [58]. The output spectral amplitude and phase stability are quantified using the complex first-order degree of coherence and its wavelength domain average (Eqs. (3) and (4), respectively, where angular brackets denote the ensemble average) [6,59]. Both are defined over the interval [0; 1], with 1 indicating perfect coherence.

$$\left|g_{12}^{(1)}(\lambda, t_a - t_b)\right| = \left|\frac{\langle\tilde{A}_a^\star(\lambda, t_a)\tilde{A}_b(\lambda, t_b)\rangle}{\sqrt{\langle|\tilde{A}_a(\lambda, t_a)|^2\rangle\langle|\tilde{A}_b(\lambda, t_b)|^2\rangle}}\right|_{a\neq b} \tag{3}$$

$$\langle|g_{12}^{(1)}|\rangle = \frac{\int_0^\infty |g_{12}^{(1)}|\langle|\tilde{A}(\lambda)|^2\rangle d\lambda}{\int_0^\infty \langle|\tilde{A}(\lambda)|^2\rangle d\lambda} \tag{4}$$

We analyze the polarization state of each output pulse using the orientation, $\theta(T)$, and ellipticity, $\psi(T)$, given by Eqs. (5) and (6), respectively. The orientation refers to the semi-major axis of the ellipse and can vary between $[-45°; 135°]$ (see Appendix C). $\psi(T)$ can vary between $[0°; 45°]$, corresponding to linear and circular polarization, respectively. $\delta(T) = \phi_x(T) - \phi_y(T)$ is the phase difference between the x- and y-polarized components, $A_x(T)$ and $A_y(T)$. $a(T)$ and $b(T)$ are magnitudes of the field on the semi-major and semi-minor axes given by Eqs. (7) and (8), respectively, and $|A(T)| = \sqrt{|A_x(T)|^2 + |A_y(T)|^2}$ is the magnitude of the field.

$$\theta(T) = \frac{1}{2}\arctan\left[\frac{2|A_x(T)||A_y(T)|\cos(\delta(T))}{|A_x(T)|^2 - |A_y(T)|^2}\right] \tag{5}$$

$$\psi(T) = \arctan\left[\frac{b(T)}{a(T)}\right] \tag{6}$$

$$a(T) = |A(T)|\sqrt{\frac{1 + \sqrt{1 - \sin^2(2\theta(T))\sin^2(\delta(T))}}{2}} \tag{7}$$

$$b(T) = |A(T)| \sqrt{\frac{1 - \sqrt{1 - \sin^2(2\theta(T))\sin^2(\delta(T))}}{2}} \tag{8}$$

We use the construction on the right of Fig. 1 to provide a visual representation of the polarization at a single isolated (snapshot) time T_S. While θ, ψ, and their statistics are well defined, the ellipses shown are an approximation of the path traced by the field $\vec{A} = \hat{x}A_x + \hat{y}A_y$ over an optical cycle (see Appendix D). The ellipses are not used to analyze the polarization data. This representation is chosen because the Poincaré sphere is often difficult to interpret in print.

$$\sigma_\theta(T) = \sqrt{\frac{1}{60} \sum_{j=1}^{60} [\theta_j(T) - \langle\theta(T)\rangle]^2} \tag{9}$$

$$\langle\sigma_\theta\rangle = \frac{\int_{-\infty}^{\infty} \sigma_\theta(T)\langle|A(T)|^2\rangle dT}{\int_{-\infty}^{\infty} \langle|A(T)|^2\rangle dT} \tag{10}$$

The ensemble orentation stability is quantified using the standard deviation, $\sigma_\theta(T)$ (Eq. (9), where j is the pulse number in the ensemble). To draw a direct comparison between the time domain polarization noise and spectral domain coherence, we remove the time dependence of $\sigma_\theta(T)$ by averaging over the time domain to get $\langle\sigma_\theta\rangle$ (Eq. (10)). We analyse the stability of the ellipticity, $\psi(T)$, in the same way by using equivalent definitions for its standard deviation, $\sigma_\psi(T)$, and average over the time domain, $\langle\sigma_\psi\rangle$. Perfect polarization stability over the ensemble is indicated by $\langle\sigma_\theta\rangle = 0°$ and $\langle\sigma_\psi\rangle = 0°$ (i.e., the standard deviation of the orientation and ellipticity is $0°$ for all T).

3. Nonlinear polarization dynamics for femtosecond pump pulses

ANDi supercontinuum generation is generally driven by optical wavebreaking when pumped using femtosecond pulses [6] so, in this section, we investigate the polarization dynamics of femtosecond pulses propagating through 1 m of PCF with a small orientation and zero birefringence to isolate nonlinear polarization effects from linear effects.

Figure 2 shows how optical wavebreaking results in deterministic nonlinear polarization dynamics. An ensemble of 200 fs input pulses is shown on the left. The input peak power is 8 kW with a ratio of 23 dB between P_x and P_y (top left, spectrum bottom left), chosen because it is representative of commercial Yb-fiber lasers. A_x and A_y have the same initial phase, expressed as the chirp (top right) using $\lambda(T) = \lambda_0 \div [1 - (\lambda_0/2\pi c)\partial\phi(T)/\partial T]$, chosen because the derivative means the chirp has a greater sensitivity to noise than the phase, increasing the visibility of noise contributions and making it easier to identify the effects of each nonlinear process. The intensity ratio and zero phase difference imply a linear polarization state ($\psi(T) = 0°$) with $\theta(T) = 4°$, visualized bottom right for $T_S = 0$ ps. $\langle\sigma_\theta\rangle$ and $\langle\sigma_\psi\rangle$ are negligible ($\sim 10^{-7}$ degrees), and therefore the ellipses of the 60 pulses are indistinguishable.

The right-hand side of Fig. 2 shows the ensemble after 1 m of PCF. The amplitude and phase profiles are modified through a combination of optical wavebreaking and XPM. Hence, the polarization parameters evolve nonlinearly through Eqs. (5) to (8), and vary significantly over the duration of the pulse [60,61]. This is demonstrated by the ellipses (bottom right, $T_S = 1.3$ ps), for which $\theta = 5.1°$ and $\psi = 2.5°$. These ellipses are indistinguishable because wavebreaking and XPM are coherent processes for short pump pulses ($\langle|g_{12}^{(1)}|\rangle \approx 1$ after 1 m of PCF), so the amplitude, phase, and therefore the orientation and ellipticity are not affected by quantum noise. As a result, the shot-to-shot polarization dynamics are stable even though the intra-pulse polarization has changed due to nonlinear polarization evolution, which happens coherently for optical wavebreaking.
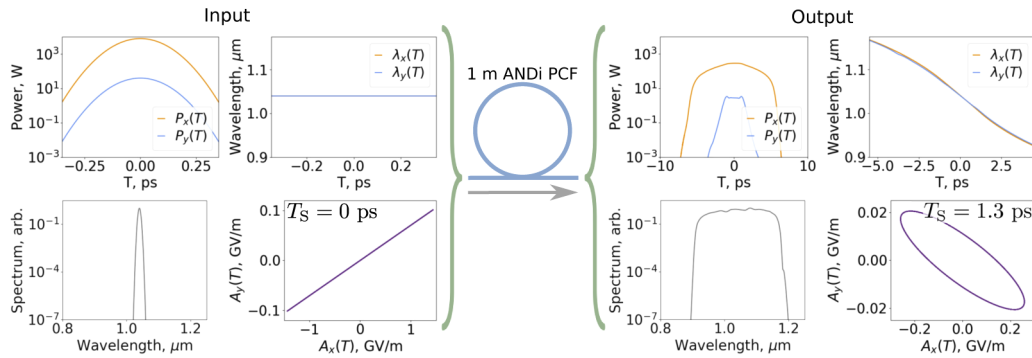
Fig. 2. Deterministic polarization evolution due to wavebreaking. 200 fs, 8 kW transform limited linearly polarized Gaussian pulses with a 4° angle with respect to a principal fiber axis undergo wavebreaking in 1 m of ANDi PCF with $\Delta\beta_1 = 0$ ps/m. Input (left): Pulses top left, spectra bottom left, phase (expressed as the chirp) top right, polarization ellipses at snapshot time $T_S = 0$ ps bottom right. Output (right): The noise-insensitive, deterministic nonlinear polarization dynamics are dominated by differences in the temporal shapes of A_x and A_y, and there is only a small difference in their chirps. The orientation and ellipticity are illustrated for each pulse in the ensemble in the bottom right (snapshot time $T_s = 1.3$ ps, where the polarization state is strongly modified).

The full temporal evolution of $\theta(T)$ and $\psi(T)$ is shown for the ensemble in Fig. 3 alongside the ensemble average output pulse shape, $\langle P(T) \rangle$. The combined effect of wavebreaking and XPM increases the maximum polarization orientation and ellipticity from 4° and 0° to 6.1° and 3.2°, respectively. Self-steepening displaces the central turning point of both θ and ψ from the origin to $T = 0.35$ ps. Repeating these simulations with a small amount of birefringence or changing the ellipticity of the input pulses does change the propagation dynamics in detail because of the redistribution of energy between A_x and A_y and the 2/3 scaling of XPM with respect to SPM. However, because these effects and the resulting nonlinear polarization evolution occur coherently when using femtosecond pump pulses, changing these parameters does not result in a change in either the coherence or the polarization statistics.
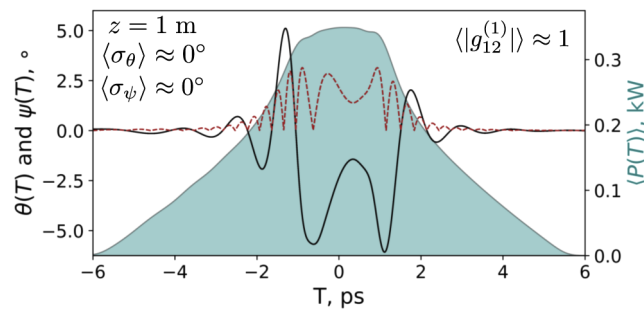

Fig. 3. $\theta(T)$ (black solid), $\psi(T)$ (red dashed), and the ensemble average of $P(T)$ (teal shading) for the ensemble after 1 m of PCF. The individual shots are indistinguishable on this scale. Visualization 1 shows the polarization dynamics of the output ensemble.

Figure 3 shows that the orientation tends to 0° for $T < -3.5$ ps at the pulse leading edge and $T > 3$ ps at the trailing edge despite the starting value of 4°. This is because of the greater spectral broadening of A_x than A_y caused by the 2/3 scaling of XPM versus SPM, and because A_x drives the nonlinear interaction. This causes A_x to disperse more quickly than A_y, with output durations

of 5.5 ps and 2.7 ps, respectively, so that $A(T) \approx A_x(T)$ at the pulse edges (see the output temporal profiles of A_x and A_y in Fig. 2). The full ensemble dynamics of $\theta(T)$, $\psi(T)$, and the ellipses are shown in Visualization 1.

4. Nonlinear polarization dynamics for picosecond pump pulses

When using few-kW peak power picosecond pump pulses, ANDi supercontinuum generation is driven primarily by Raman-assisted parametric FWM, XPM-assisted Raman amplification, and secondarily by SPM and self-steepening [6,19]. Here, we investigate the polarization dynamics of 7 ps, 8 kW Gaussian pulses with $\theta = 4°$ propagating in ANDi PCF with zero birefringence as in section 3. All input pulse parameters are the same as for Figs. 2 and 3 except for the duration and energy (60 nJ). $\langle \sigma_\theta \rangle$ and $\langle \sigma_\psi \rangle$ are negligible at the fiber input ($\sim 10^{-7}$ degrees).

Figure 4 shows the ensemble after 1 m of PCF. Each shot shows stochastic time and wavelength domain modulations (top row) as well as chirp noise (bottom left) where Raman amplification is significant in the time domain (−5 ps to 1.5 ps). As in section 3, the nonlinear amplitude and phase modulations transfer directly to both the polarization ellipticity and orientation. The ellipses (bottom right) visualize θ and ψ for each shot at $T_S = -3.4$ ps (where Raman amplification is strongest). The nonlinear amplitude and phase modulations are incoherent where Raman amplification dominates, so the intra-pulse polarization dynamics between −5 ps and 1.5 ps are highly sensitive to quantum noise and are no longer deterministic.
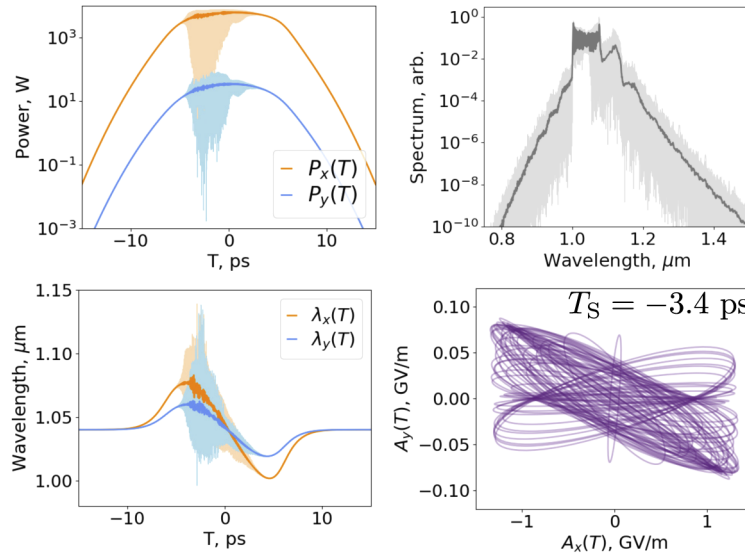

Fig. 4. 7 ps, 8 kW transform limited linearly polarized Gaussian pulses after propagating through 1 m of ANDi PCF with $\Delta\beta_1 = 0$ ps/m. Top left: time domain. Top right: wavelength domain. Bottom left: chirp. Bottom right: polarization. Incoherent Raman amplification has resulted in stochastic modulations in the temporal and spectral domains as well as the chirp. The noise contributions to A_x and A_y are different, randomizing the polarization where incoherent Raman amplification is strongest (−3.4 ps).

By setting $\Delta\beta_1 = 0$ ps/m, A_x and A_y remain temporally overlapped for the full fiber length, and so the polarization noise occurs at the same propagation distance as the Raman-based decoherence. This is shown in the left-hand plot of Fig. 5, where $\langle \sigma_\theta \rangle$ and $\langle \sigma_\psi \rangle$ are shown with $\langle |g_{12}^{(1)}| \rangle$ as a function of z, confirming that polarization noise is intrinsically linked to Raman-based

decoherence. The stable and linear input polarization state becomes highly sensitive to noise for just a modest reduction in $\langle|g_{12}^{(1)}|\rangle$ from ~ 1 to 0.81 over 1 m of PCF.
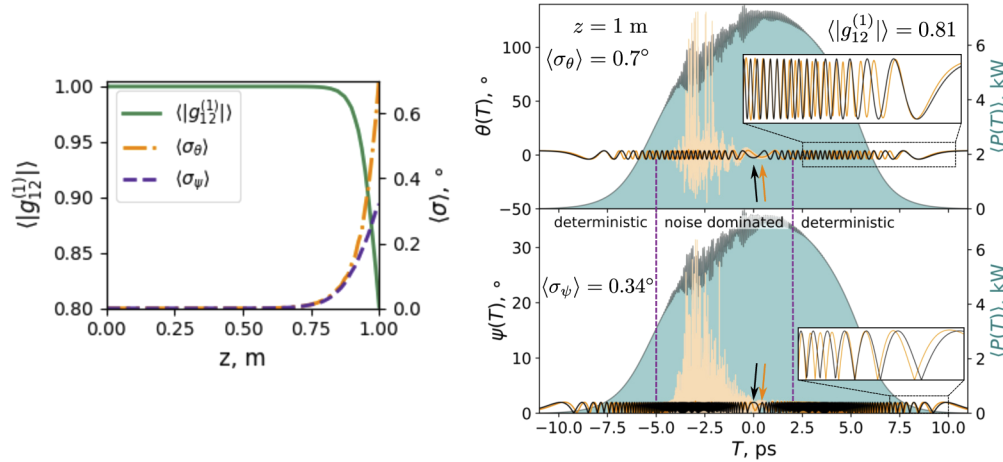

Fig. 5. Left: $\langle|g_{12}^{(1)}|\rangle$, $\langle\sigma_\theta\rangle$, and $\langle\sigma_\psi\rangle$ as a function of z for the ensemble shown in Fig. 4. Right top and bottom: $\theta(T)$, $\psi(T)$, and the ensemble average of $P(T)$ (teal shading) at $L = 1$ m. θ and ψ for the individual pulses, ensemble average, and analytic calculation are shown by the pale orange, dark orange, and black lines, respectively. Insets: The analytic theory and the simulation match closely where Raman is not significant. Arrows: Displacement of the central turning points due to self-steepening. Visualization 2 shows how the ensemble polarization state varies with T.

The right-hand plots in Fig. 5 show the ensemble temporal evolution of $\theta(T)$ (top) and $\psi(T)$ (bottom). The severity of the polarization noise between -5 ps and 1.5 ps is clear: $\theta(T)$ and $\psi(T)$ span $-44.7°$ to $134.9°$ (close to the full range) and $0°$ to $31°$, respectively, indicating complete depolarization where Raman effects dominate (between the vertical purple dashed lines). In this region, $\max(\sigma_\theta(T)) = 35°$, $\max(\sigma_\psi(T)) = 8°$, giving $\langle\sigma_\theta\rangle = 0.71°$ and $\langle\sigma_\psi\rangle = 0.34°$ over the entire pulse. $\langle P(T)\rangle$ (right axis) verifies that Raman and the depolarization coincide in the time domain. Further simulations in which we increase the pulse duration, energy, or propagation distance result in complete destruction of the pulse coherence due to Raman amplification and thus expand the noise-dominated region beyond this range and cause $\langle\sigma_\theta\rangle$ and $\langle\sigma_\psi\rangle$ to increase.

The orientation and ellipticity of each pulse remains insensitive to quantum noise where Raman does not dominate, leaving deterministic polarization regions in the pulse wings. $\max(\sigma_\theta(T))$ and $\max(\sigma_\psi(T))$ are approximately 10^{-5} degrees in these regions. The polarization evolution there is characterised by coherent ultrafast oscillations in $\theta(T)$ and $\psi(T)$, caused by beating between the phase contribution from SPM in A_x and XPM in A_y. This process is similar to the coherent nonlinear polarization evolution seen with the femtosecond results above, but with the picosecond pulses the peak power remains high over the full fiber length due to negligible dispersion and the absence of wavebreaking, so the accumulated nonlinear phase mismatch from SPM and XPM is significantly larger in comparison with the femtosecond pulse ensemble (~ 340 rad and ~ 65 rad, respectively). This leads to the larger oscillation frequency of the orientation and ellipticity for picosecond pump pulses.

We confirm that SPM and XPM are responsible for the coherent oscillations in θ and ψ in the pulse wings by solving Eqs. (5) and (6) analytically (solid black lines, Fig. 5). We define $\delta(T)$ using Eq. (11) with the same fiber and pulse parameters as in the simulations. Equation (11) is valid where SPM and XPM are the only contributors to the phase mismatch and where A_x drives the nonlinear interaction. The analytic results closely match the simulation, with amplitudes

agreeing to within 5% and the two approaches yielding approximately equal oscillation periods.

$$\delta(T) = \frac{-1}{3}\gamma|A_x(T)|^2 L \tag{11}$$

Differences visible in the insets are attributed to dispersive and self-steepening effects, which are included in the simulations but not in the analytic calculation. Self-steepening causes the difference in position of the turning point of θ and ψ along the T-axis (at 0 ps for the analytic calculation but 0.44 ps for the simulation, black and orange arrows, respectively). To illustrate the deterministic and noise dominated polarization regimes (and the transitions between them), the full ensemble dynamics of $\theta(T)$ and $\psi(T)$ are shown for T between ±10 ps in Visualization 2.

5. Competition between wavebreaking and Raman amplification

The competition between optical wavebreaking and Raman-assisted parametric FWM determines the coherence of the supercontinuum process in the normal dispersion regime [6]. Both this competition and the coherence are parameterised by the ratio of $L_R^\star$ to L_{WB} (see Eqs. (2)), and so longer pump pulses for which Raman amplification dominates result in a lower coherence than shorter pump pulses with the same peak power. In this section we study the effect of XPM by simulating the ensemble polarization statistics as the propagation dynamics are changed from coherent to incoherent, and extend the discussion in sections 3 and 4 to include the fiber birefringence.

We have calculated $\langle|g_{12}^{(1)}|\rangle$, $\langle\sigma_\psi\rangle$, and $\langle\sigma_\theta\rangle$ over a broad range of polarization GVM ($\Delta\beta_1$), pulse energy and duration values while keeping the peak power fixed at 15 kW (approximating values commonly used in experiments and simulations [4,6,8,19]). This higher peak power means that the polarization dynamics can be observed for ensembles with much lower output coherence than in sections 3 and 4. We parameterize the pulse characteristics using N_{pump} (Eq. (1)) and the constant peak power gives $L_N = 2.5$ mm ($\gamma P_0 = 405$ rad/m). The pulse duration and energy range from 0.1 ps to 9 ps and 1.6 nJ to 140 nJ, respectively, giving $L_R^\star = 0.1$ m and varying L_{WB} from 4 cm to 3.4 m, permitting both coherent and incoherent dynamics. L_D spans 0.56 m to 4.3 km, and N spans 15 to 1313. The ratio of P_x to P_y is 23 dB (linear polarization and $\theta = 4°$ as in sections 3 and 4), and the GVM has values between ±2 ps/m.
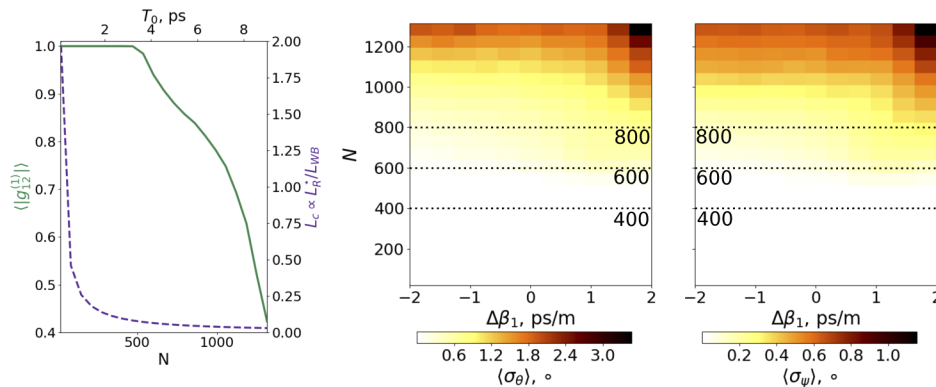

Fig. 6. Polarization dynamics for coherent and incoherent spectral broadening in birefringent ANDi fiber. Left: $\langle|g_{12}^{(1)}|\rangle$ (Eq. (4), left axis) and $L_R^\star/L_W$ (Eqs. (2), right axis, dashed line) as a function of N (Eq. (1)) and T_0. Center and right: $\langle\sigma_\theta\rangle$ and $\langle\sigma_\psi\rangle$, showing a monotonic increase in polarization noise with N. The polarization noise is maximized when the dominant polarization component (A_x) travels slower ($\Delta\beta_1 > 0$ ps/m) because this maximizes the overlap of A_y with the Raman amplification at the leading edge of A_x.

The coherence degradation is shown as a function of N and T_0 in the top row of Fig. 6 (left vertical axis) for non-birefringent fiber only because $\langle|g_{12}^{(1)}|\rangle$ shows no GVM dependence. The ratio $L_R^\star/L_{WB}$ is shown by the dashed line (right vertical axis), and shows that Raman amplification becomes the dominant nonlinear effect between $N = 400$ and 600, below which the short pulse durations maintain $\langle|g_{12}^{(1)}|\rangle \geq 0.9$ (i.e., coherent propagation). The bottom left and right plots of Fig. 6 show $\langle\sigma_\theta\rangle$ and $\langle\sigma_\psi\rangle$ as a function of N and GVM ($\Delta\beta_1$). Coherent propagation (low values of N) corresponds to deterministic polarization dynamics (low values of $\langle\sigma\rangle$) for $N \leq 400$. In this region, both $\langle\sigma_\theta\rangle$ and $\langle\sigma_\psi\rangle$ are below 10^{-3} degrees.

For $N>600$, the decoherence coincides with polarization ellipticity and orientation noise as Raman amplification becomes dominant ($L_R^\star/L_{WB}<0.1$ and $\langle|g_{12}^{(1)}|\rangle<0.9$). The relationship between the coherence and polarization noise is monotonic, and only weakly dependent on the polarization GVM for $N<800$ (where $\langle\sigma_\theta\rangle<0.73°$ and $\langle\sigma_\psi\rangle<0.35°$).

The influence of the GVM on the polarization noise is most significant for $N>800$, and is maximized when the dominant polarization component (A_x) travels slower than the weaker component (A_y), i.e., when $\Delta\beta_1>0$ ps/m. This ensures that the temporal overlap of A_y with the incoherent leading edge of A_x is maximized, increasing the amplitude and phase noise of A_y [19] and thus leading to very significant polarization noise. For example, when $N = 1313$ and $\Delta\beta_1 = -2$ ps/m so that the dominant polarization component travels faster, $\langle\sigma_\theta\rangle = 1.9°$ and $\langle\sigma_\psi\rangle = 0.65°$. For the opposite case ($\Delta\beta_1 = 2$ ps/m) these increase to 3.5° and 1.2°, respectively. Hence, Raman-based polarization noise is reduced when the pulse is polarized primarily along the low index axis, and the reduction to the lowest levels would be expected in PM as opposed to non-PM fiber.

6. Distinction from cross-phase and polarization modulation instability

Cross-phase modulation instability (MI) is a process in which noise present in an optical signal is amplified rapidly by XPM between polarization components [62], causing both decoherence and polarization noise. The cross-phase MI frequency detuning and gain bandwidth have values of order 1 THz [60], determined by a phase matching condition involving the birefringence, dispersion, and the peak power through a nonlinear phase contribution [63]. Cross-phase MI amplifies out-of-band noise when the gain is not adequately saturated by the wings of the pulse spectrum and when both polarization axes are excited, i.e., when the pulse bandwidth is narrow (picosecond duration or longer) and when $\theta = 45°$. It has been shown that cross-phase MI is suppressed in birefringent fibers when the peak power exceeds a threshold, P_{th} (Eq. (12)), beyond which the phasematching condition is no longer met [63]:

$$P_{th} = \frac{3(\Delta\beta_1)^2}{4\beta_2\gamma} \qquad (12)$$

Cross-phase MI in the normal dispersion regime is well documented [27], and the effect has been included in our simulations (see Appendix A). However, we have isolated the propagation regimes in sections 3, 4, and 5 from that in which cross-phase MI plays a strong role by using pulses with only a small polarization offset from a principal fiber axis.

Two key distinctions exist between our observed Raman-based polarization noise and that caused by cross-phase MI. Firstly, we have shown in sections 4 and 5 that, unlike cross-phase MI, the onset of Raman-based polarization noise does not require a significant polarization misalignment from a principal fiber axis (see Appendix E, where we show that polarization noise still occurs for a ratio of P_x to P_y of 43 dB). Polarization noise is significant for both high and low birefringence fibers for a broad range of pulse parameters in the data shown in Fig. 6. Secondly, the Raman-based polarization noise is not subject to a peak power threshold. As an example, $P_{th} = 5.6$ kW for the simulations where $\Delta\beta_1 = 2$ ps/m (Eq. (12)), which is approximately three

times smaller than the peak powers used in this work. The polarization noise is therefore expected to be negligible for this GVM when only cross-phase MI is considered. This is in direct contrast with the Raman-based polarization noise, which is instead maximized for this GVM by the improved overlap of the weaker polarization component with the incoherent leading edge of the dominant component (see section 5).

In addition to cross-phase MI, polarization MI in low birefringence ANDi fiber has also been shown to result in polarization noise and decoherence in femtosecond pulses [24]. As with cross-phase MI, polarization MI only occurs where phasematching conditions set by the fiber birefringence, dispersion, and the pulse peak power are met, resulting in a reduction in the severity of polarization MI-induced decoherence and polarization noise for high birefringence fibers [21,60]. This is not the case for Raman-based polarization noise in picosecond pulses, which varies slowly with fiber birefringence and is maximimized for high birefringence fiber when the pulse is primarily polarized along the slow axis (shown in Fig. 6).

7.   Conclusion

We have explored the intra-pulse polarization dynamics of both coherent wavebreaking and incoherent Raman amplification in ANDi supercontinuum generation by considering sub-20 kW linearly polarized pulses with a small angular offset from a principal fiber axis. We have shown that the polarization orientation and ellipticity exhibit periodic and deterministic dynamics (i.e., not influenced by quantum noise) where nonlinear propagation is dominated by elastic processes such as SPM, wavebreaking, self-steepening, and dispersion, and that the polarization becomes highly unstable where incoherent broadening processes dominate.

We find that even for strongly polarized input pulses both the orientation and ellipticity of the polarization becomes highly sensitive to quantum noise for just a moderate reduction in the coherence where incoherent Raman-assisted parametric FWM and XPM-assisted Raman amplification dominate. Unlike polarization noise associated with cross-phase MI, this process is found to have no power threshold for a given GVM and is maximized when the weaker polarization component has a higher group velocity. Conversely, polarization noise is reduced (but not fully prevented) when the high energy component propagates along the low index axis of the fiber; this approach to reducing polarization noise is most effective for highly birefringent fiber. Polarization noise should therefore be anticipated for ANDi supercontinuum experiments employing either non-PM or PM fiber once incoherent broadening occurs. Additionally, Appendix E shows that polarization noise is significant even for very strongly polarized input pulses. We anticipate that our findings will be experimentally observable with the development of a broadband, single shot extension of any existing polarization- and field-resolved pulse retrieval technique [64–66].

These observations may aid the development of other pulsed light sources, such as the intracavity dynamics of Raman-based noise-like pulse generation in ANDi fiber lasers which use nonlinear polarization evolution gating [36]. These sources can produce coherent modelocked or incoherent noise-like pulse trains depending on the cavity polarization control [36], which bears similarities to our observation that the severity of the polarization noise depends on whether the pulse is polarized along the low or high index axis. Additionally, our observations are expected to be relevant to investigations of non-silica fibers, especially those with stronger nonlinear indices or Raman contributions than fused silica, such as gas and liquid core fibers [43–45,49,67] and ANDi fibers targeted for infra-red pumping [15,50–52,68]. Developments in these fields would benefit applications such as frequency metrology [11], short-wavelength and ultrafast pulse generation [3,41,69], spectroscopy [40], microscopy [13], and noise-like pulse generation for applications which do not require a high degree of coherence [70].

Appendix A. Polarization-resolved generalized nonlinear Schrödinger equation

The pulse propagation is simulated using the generalized nonlinear Schrödinger equation (GNLSE) shown by Eq. (13).

$$\frac{\partial A(z,T)}{\partial z} = [\hat{L}(T) + \hat{N}(T)]A(z,T) \tag{13}$$

Solutions are found in the frequency domain [71] using the integration and adaptive step sizing methods outlined in [72] and [73], respectively. $\hat{L}$ and $\hat{N}$ are linear and nonlinear operators, shown by Eqs. (14) and (15). Polarization dynamics are included using $A(z,T) = \hat{x}A_x(z,T) + \hat{y}A_y(z,T)$ and Jones calculus [74] to apply the linear and nonlinear operators to A_x and A_y because this method has been shown to reproduce complex polarization dynamics in nonlinear fiber systems accurately [75] ($\hat{x}$ and $\hat{y}$ are orthogonal unit vectors along the fiber birefringence axes). $\Omega = \omega - \omega_0$ is the angular frequency grid centered at 0 THz and T is the retarded time frame comoving with A_x, given by $T = t - z/v_{gx}$ where v_{gx} is the group velocity of A_x.

$$\hat{\tilde{L}}(\Omega) = \frac{\alpha(\Omega)}{2} - i\left[\Delta\beta_1\Omega - \frac{\beta_2(\Omega)}{2}\Omega^2\right] \tag{14}$$

$$\hat{N}_x(T) = -i\gamma\left(1 + \frac{1}{\omega_0}\frac{\partial}{\partial T}\right) \times \left[(1 - f_R)\left(|A_x|^2 + \frac{2}{3}|A_y|^2\right)\right.$$
$$\left. + f_R\int_0^\infty h_R(\tau)\sum_{j=x,y}|A_j(T-\tau)|^2 d\tau + i\Gamma_R\right] \tag{15}$$

The linear operator, $\hat{\tilde{L}}(\Omega)$ (frequency domain, Eq. (14)), includes the full fiber dispersion profile ($\beta_2(\Omega)$), loss ($\alpha(\Omega)$), and the polarization GVM ($\Delta\beta_1$). Our definition of T sets $\beta_1 = 0$ ps/m for A_x, and $\Delta\beta_1 = \beta_{1x} - \beta_{1y}$ for A_y (where $\beta_1 = 1/v_g$). This centered A_x at $T = 0$ ps in all of the simulations while allowing A_y to be advanced ($\Delta\beta_1 > 0$ ps/m) or delayed ($\Delta\beta_1 < 0$ ps/m) with respect to A_x.

The nonlinear operator ($N_x(T)$, Eq. (15)) accounts for self-steepening, SPM, XPM and cross-phase MI, and Raman scattering via $h_R(\tau)$, which is the Raman response of fused silica. (We omit the field dependence on z and T for brevity). Γ_R accounts for spontaneous Raman scattering [58]. We did not include the orthogonal component of the Raman gain in our model because it has a peak value which is much smaller than that of the parallel component, so it contributes negligibly to the amplification of quantum noise. This approximation also helped to reduce execution time by requiring fewer fast Fourier transforms (FFTs) when applying the nonlinear operator. $N_y(T)$ is obtained by swapping A_x and A_y in Eq. (15).

Appendix B. Scaling propagation simulations for large ensemble sizes

An ensemble size of 60 pulses has been chosen so that the polarization statistics are reliable, resulting in large simulation sizes of 120 GNLSEs per ensemble (two coupled GNLSEs per pulse, or one for each polarization component). The analysis in section 5, for example, required 27,720 GNLSEs to be solved in total, with each having 2^{15} time-frequency grid points. This necessitated large-scale parallelization of our code so that we could use small propagation step sizes for high accuracy while maintaining a reasonable execution time, which is achieved in our case using general purpose graphical processing units and the arrayfire library [76] for vectorised mathematical operations. We further reduced the simulation runtime by using the FFTW3 library [77] in a few cases where it was necessary to perform FFTs on a CPU to reduce communication overheads (when, for example, only one FFT of a single pulse was required).

Appendix C. Defining the polarization ellipse orientation

The calculation of the polarization ellipse orientation using Eq. (5) in section 2 means $\theta(T)$ takes maximum values of $\pm45°$ from the fiber x-axis. Using this calculation alone would result in an incomplete representation of the orientation because A_y-dominant states would be indistiguishable from A_x-dominant states in our model (i.e., the orientation is ambiguous as it refers to either the semi-major or semi-minor ellipse axis).

To resolve this ambiguity, we use Eqs. (16) and (17) to adjust θ based on the relative magnitudes of the field envelopes at angles θ and $\theta \pm 90°$ (T-dependence omitted for brevity).

$$A_1 = \left[|A_x|^2\cos^2(\theta) + |A_y|^2\sin^2(\theta) + |A_x||A_y|\cos(\delta)\sin(2\theta) \right]^{1/2} \tag{16}$$

$$A_2 = \left[|A_x|^2\sin^2(\theta) + |A_y|^2\cos^2(\theta) - |A_x||A_y|\cos(\delta)\sin(2\theta) \right]^{1/2} \tag{17}$$

When $A_2 > A_1$, θ defines the angle subtended by the semi-minor axis, and so we add 90° to the orientation whenever this is the case to ensure that the orientation is always defined using the semi-major axis. Additionally, we assume that the polarization state is degenerate under a rotation of 180°. This is permitted because we consider pulses with durations much larger than a few optical cycles and because the temporal resolution of our simulations (4.2 fs) is larger than the field period at λ_0 (3.47 fs). Our model thus incorporates all A_x- and A_y-dominant polarization states in addition to those with $|A_x| = |A_y|$.

Appendix D. Visualizing the polarization state

Our orientation and ellipticity calculations (and subsequent statistical analyses) are well defined for all isolated points ('snapshots') in time, T_S, in our model. However, because the GNLSE invokes the slowly-varying envelope approximation we choose to use the ellipse representation to provide an approximate and intuitive visualization of the orientation and ellipticity. Ellipses are chosen instead of the Poincaré sphere because this three-dimensional representation can be difficult to interpret in print.

The visualisations of the orientation and ellipticity are plotted parametrically in cartesian coordinates, (x, y). First, we define an array ζ which takes on values between $\pm\pi$ in steps of $\pi/512$. We then set the ellipse x and y axes equal to $A_x(T_S)\cos[\zeta + \phi_x(T_S)]$ and $A_y(T_S)\cos[\zeta + \phi_y(T_S)]$, respectively, where $\phi_x(T_S)$ and $\phi_y(T_S)$ are the phase angles of the polarization components $A_x(T)$ and $A_y(T)$ at snapshot time T_S. The resulting orientation and ellipticity correspond to the real values at time T_S. Array ζ is included so that a full ellipse is plotted rather than just the vector $\vec{A}(T_S) = \hat{x}A_x(T_S) + \hat{y}A_y(T_S)$, because this would not show the ellipticity of the field at time T_S.

Appendix E. Influence of polarization misalignment from a principal fiber axis

Throughout this work we have chosen input pulses for which the polarization ellipse semi-major axis is misaligned from a principal fiber axis by 4° by setting $|A_x|^2/|A_y|^2 = 200$ (peak power ratio of 23 dB). This is representative of many commercial fiber laser systems. Here, for completeness, we extend the investigation of Raman-based polarization noise to include different polarization misalignments.

Figure 7 shows how $\langle \sigma_\theta \rangle$ and $\langle \sigma_\psi \rangle$ are affected when the input polarization misalignment from the fiber x-axis takes values of 6° ($|A_x|^2/|A_y|^2 = 100$; peak power ratio of 20 dB), 4° ($|A_x|^2/|A_y|^2 = 200$; peak power ratio of 23 dB), and 0.4° ($|A_x|^2/|A_y|^2 = 2 \times 10^4$; peak power ratio of 43 dB). All other parameters are the same as those used in Fig. 4. The polarization noise is shown as a function of fiber length alongside the average coherence, $\langle |g_{12}| \rangle$ (green solid curve, left axis), which is approximately the same for each input orientation because of the constant peak power of 8 kW.
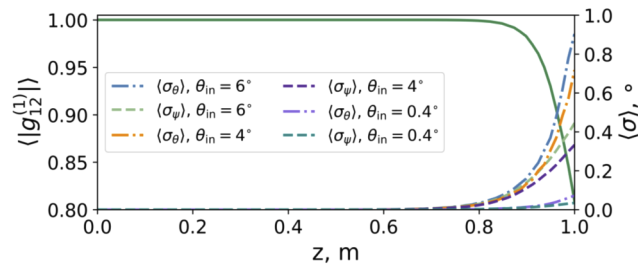
Fig. 7. Average coherence (green solid, left axis) and average polarization statistics for peak power ratios of 20, 23, and 43 dB (right axis). Increasing the polarization misalignment from a principal fiber axis increases the polarization noise.

As expected, increasing the misalignment of the initial ellipse orientation from a principal fiber axis increases the polarization noise. Each ensemble starts with $\langle\sigma\rangle \approx 10^{-7}$ degrees, but after 1 m of PCF $\langle\sigma_\theta\rangle = 0.9°, 0.7°$, and $0.06°$ for input peak power ratios of 20, 23, and 43 dB, respectively. The respective ellipticity statistics follow a similar trend: $\langle\sigma_\psi\rangle = 0.42°, 0.34°$, and $0.02°$. Hence, although reduced for lower orientation misalignments, the polarization noise is significant even for strongly polarized sources. The variation is attributed to the greater influence of the noise-seeded Raman bands on A_y when the energy of this polarization component is increased.

Funding

Acknowledgments

Disclosures

The authors declare no conflicts of interest.

References

1. P. Falk, M. H. Frosz, and O. Bang, "Supercontinuum generation in a photonic crystal fiber with two zero-dispersion wavelengths tapered to normal dispersion at all wavelengths," Opt. Express **13**(19), 7535–7540 (2005).
2. L. E. Hooper, P. J. Mosley, A. C. Muir, W. J. Wadsworth, and J. C. Knight, "Coherent supercontinuum generation in photonic crystal fiber with all-normal group velocity dispersion," Opt. Express **19**(6), 4902–4907 (2011).
3. I. A. Sukhoivanov, S. O. Iakushev, O. V. Shulika, J. A. Andrade-Lucio, A. Díez, and M. Andrés, "Supercontinuum generation at 800 nm in all-normal dispersion photonic crystal fiber," Opt. Express **22**(24), 30234–30250 (2014).
4. A. M. Heidt, A. Hartung, G. W. Bosman, P. Krok, E. G. Rohwer, H. Schwoerer, and H. Bartelt, "Coherent octave spanning near-infrared and visible supercontinuum generation in all-normal dispersion photonic crystal fibers," Opt. Express **19**(4), 3775–3787 (2011).
5. J. M. Dudley, G. Genty, and S. Coen, "Supercontinuum generation in photonic crystal fiber," Rev. Mod. Phys. **78**(4), 1135–1184 (2006).
6. A. M. Heidt, J. S. Feehan, J. H. V. Price, and T. Feurer, "Limits of coherent supercontinuum generation in normal dispersion fibers," J. Opt. Soc. Am. B **34**(4), 764–775 (2017).
7. W. J. Tomlinson, R. H. Stolen, and A. M. Johnson, "Optical wave breaking of pulses in nonlinear optical fibers," Opt. Lett. **10**(9), 457–459 (1985).

8. A. M. Heidt, "Pulse preserving flat-top supercontinuum generation in all-normal dispersion photonic crystal fibers," J. Opt. Soc. Am. B **27**(3), 550–559 (2010).
9. N. Nishizawa, Y. Chen, P. Hsiung, E. P. Ippen, and J. G. Fujimoto, "Real-time, ultrahigh-resolution, optical coherence tomography with an all-fiber, femtosecond fiber laser continuum at 1.5 μm," Opt. Lett. **29**(24), 2846–2848 (2004).
10. G. Humbert, W. J. Wadsworth, S. G. Leon-Saval, J. C. Knight, T. A. Birks, P. S. J. Russell, M. J. Lederer, D. Kopf, K. Wiesauer, E. I. Breuer, and D. Stifter, "Supercontinuum generation system for optical coherence tomography based on tapered photonic crystal fibre," Opt. Express **14**(4), 1596–1603 (2006).
11. R. Holzwarth, T. Udem, T. W. Hänsch, J. C. Knight, W. J. Wadsworth, and P. S. J. Russell, "Optical Frequency Synthesizer for Precision Spectroscopy," Phys. Rev. Lett. **85**(11), 2264–2267 (2000).
12. C. R. Head, H. Y. Chan, J. S. Feehan, D. P. Shepherd, S. Alam, A. C. Tropper, J. H. V. Price, and K. G. Wilcox, "Supercontinuum Generation With GHz Repetition Rate Femtosecond-Pulse Fiber-Amplified VECSELs," IEEE Photonics Technol. Lett. **25**(5), 464–467 (2013).
13. K. P. Herdzik, K. N. Bourdakos, P. B. Johnson, A. P. Lister, A. P. Pitera, C.-Y. Guo, P. Horak, D. J. Richardson, J. H. V. Price, and S. Mahajan, "Multimodal spectral focusing CARS and SFG microscopy with a tailored coherent continuum from a microstructured fiber," Appl. Phys. B **126**(5), 84 (2020).
14. J. H. V. Price, X. Feng, A. M. Heidt, G. Brambilla, P. Horak, F. Poletti, G. Ponzo, P. Petropoulos, M. Petrovich, J. Shi, M. Ibsen, W. H. Loh, H. N. Rutt, and D. J. Richardson, "Supercontinuum generation in non-silica fibers," Opt. Fiber Technol. **18**(5), 327–344 (2012).
15. S. Xing, S. Kharitonov, J. Hu, and C.-S. Brès, "Linearly chirped mid-infrared supercontinuum in all-normal-dispersion chalcogenide photonic crystal fibers," Opt. Express **26**(15), 19627–19636 (2018).
16. H. P. T. Nguyen, K. Nagasaka, T. H. Tuan, T. S. Saini, X. Luo, T. Suzuki, and Y. Ohishi, "Highly coherent supercontinuum in the mid-infrared region with cascaded tellurite and chalcogenide fibers," Appl. Opt. **57**(21), 6153–6163 (2018).
17. I. B. Gonzalo and O. Bang, "Role of the Raman gain in the noise dynamics of all-normal dispersion silica fiber supercontinuum generation," J. Opt. Soc. Am. B **35**(9), 2102–2110 (2018).
18. E. Genier, P. Bowen, T. Sylvestre, J. M. Dudley, P. Moselund, and O. Bang, "Amplitude noise and coherence degradation of femtosecond supercontinuum generation in all-normal-dispersion fibers," J. Opt. Soc. Am. B **36**(2), A161–A167 (2019).
19. J. S. Feehan and J. H. V. Price, "Decoherence due to XPM-assisted Raman amplification for polarization or wavelength offset pulses in all-normal dispersion supercontinuum generation," J. Opt. Soc. Am. B **37**(3), 635–644 (2020).
20. E. A. Golovchenko, P. V. Mamyshev, A. N. Pilipetskii, and E. M. Dianov, "Mutual influence of the parametric effects and stimulated Raman scattering in optical fibers," IEEE J. Quantum Electron. **26**(10), 1815–1820 (1990).
21. S. Trillo and S. Wabnitz, "Parametric and Raman amplification in birefringent fibers," J. Opt. Soc. Am. B **9**(7), 1061–1082 (1992).
22. S. Coen, D. A. Wardle, and J. D. Harvey, "Observation of Non-Phase-Matched Parametric Amplification in Resonant Nonlinear Optics," Phys. Rev. Lett. **89**(27), 273901 (2002).
23. H. Tu, Y. Liu, X. Liu, D. Turchinovich, J. Lægsgaard, and S. A. Boppart, "Nonlinear polarization dynamics in a weakly birefringent all-normal dispersion photonic crystal fiber: toward a practical coherent fiber supercontinuum laser," Opt. Express **20**(2), 1113–1128 (2012).
24. I. B. Gonzalo, R. D. Engelsholm, M. P. Sørensen, and O. Bang, "Polarization noise places severe constraints on coherence of all-normal dispersion femtosecond supercontinuum generation," Sci. Rep. **8**(1), 6579 (2018).
25. A. Loredo-Trejo, Y. Lòpez-Diéguez, L. Velázquez-Ibarra, A. Díez, E. Silvestre, J. M. Estudillo-Ayala, and M. V. Andrés, "Polarization Modulation Instability in All-Normal Dispersion Microstructured Optical Fibers with Quasi-Continuous Pump," IEEE Photonics J. **11**(5), 1–8 (2019).
26. Y. Liu, Y. Zhao, J. Lyngsø, S. You, W. L. Wilson, H. Tu, and S. A. Boppart, "Suppressing short-term polarization noise and related spectral decoherence in all-normal dispersion fiber supercontinuum generation," J. Lightwave Technol. **33**(9), 1814–1820 (2015).
27. G. P. Agrawal, P. L. Baldeck, and R. R. Alfano, "Modulation instability induced by cross-phase modulation in optical fibers," Phys. Rev. A **39**(7), 3406–3413 (1989).
28. H.-Y. Chan, S.-U. Alam, L. Xu, J. Bateman, D. J. Richardson, and D. P. Shepherd, "Compact, high-pulse-energy, high-power, picosecond master oscillator power amplifier," Opt. Express **22**(18), 21938–21943 (2014).
29. J. S. Feehan, J. H. V. Price, T. J. Butcher, W. S. Brocklesby, J. G. Frey, and D. J. Richardson, "Efficient high-harmonic generation from a stable and compact ultrafast Yb-fiber laser producing 100 μJ, 350 fs pulses based on bendable photonic crystal fiber," Appl. Phys. B **123**(1), 43 (2017).
30. M. E. Fermann, V. I. Kruglov, B. C. Thomsen, J. M. Dudley, and J. D. Harvey, "Self-similar propagation and amplification of parabolic pulses in optical fibers," Phys. Rev. Lett. **84**(26), 6010–6013 (2000).
31. T. N. Nguyen, K. Kieu, A. V. Maslov, M. Miyawaki, and N. Peyghambarian, "Normal dispersion femtosecond fiber optical parametric oscillator," Opt. Lett. **38**(18), 3616–3619 (2013).
32. W. Fu and F. W. Wise, "Normal-dispersion fiber optical parametric chirped-pulse amplification," Opt. Lett. **43**(21), 5331–5334 (2018).
33. N. J. Doran and D. Wood, "Nonlinear-optical loop mirror," Opt. Lett. **13**(1), 56–58 (1988).
34. M. E. Fermann, F. Haberl, M. Hofer, and H. Hochreiter, "Nonlinear amplifying loop mirror," Opt. Lett. **15**(13), 752–754 (1990).

35. A. E. Bednyakova, S. A. Babin, D. S. Kharenko, E. V. Podivilov, M. P. Fedoruk, V. L. Kalashnikov, and A. Apolonski, "Evolution of dissipative solitons in a fiber laser oscillator in the presence of strong raman scattering," Opt. Express **21**(18), 20556–20564 (2013).

36. D. Li, D. Shen, L. Li, H. Chen, D. Tang, and L. Zhao, "Raman-scattering-assistant broadband noise-like pulse generation in all-normal-dispersion fiber lasers," Opt. Express **23**(20), 25889–25895 (2015).

37. M. R. Lamont, B. Luther-Davies, D.-Y. Choi, S. Madden, X. Gai, and B. J. Eggleton, "Net-gain from a parametric amplifier on a chalcogenide optical chip," Opt. Express **16**(25), 20374–20381 (2008).

38. X. Gai, D.-Y. Choi, S. Madden, and B. Luther-Davies, "Interplay between raman scattering and four-wave mixing in As$_2$S$_3$ chalcogenide glass waveguides," J. Opt. Soc. Am. B **28**(11), 2777–2784 (2011).

39. Y. Y. Wang, N. V. Wheeler, F. Couny, P. J. Roberts, and F. Benabid, "Low loss broadband transmission in hypocycloid-core kagome hollow-core photonic crystal fiber," Opt. Lett. **36**(5), 669–671 (2011).

40. N. Kotsina, F. Belli, S.-F. Gao, Y.-Y. Wang, P. Wang, J. C. Travers, and D. Townsend, "Ultrafast molecular spectroscopy using a hollow-core photonic crystal fiber light source," J. Phys. Chem. **10**(4), 715–720 (2019).

41. J. Travers, T. Grigorova, C. Brahms, and F. Belli, "High-energy pulse self-compression and ultraviolet generation through soliton dynamics in hollow capillary fibres," Nat. Photonics **13**(8), 547–554 (2019).

42. M. A. Finger, N. Y. Joly, T. Weiss, and P. S. Russell, "Accuracy of the capillary approximation for gas-filled kagome-style photonic crystal fibers," Opt. Lett. **39**(4), 821–824 (2014).

43. M. Mlejnek, E. M. Wright, and J. V. Moloney, "Dynamic spatial replenishment of femtosecond pulses propagating in air," Opt. Lett. **23**(5), 382–384 (1998).

44. E. T. J. Nibbering, G. Grillon, M. A. Franco, B. S. Prade, and A. Mysyrowicz, "Determination of the inertial contribution to the nonlinear refractive index of air, N$_2$, and O$_2$ by use of unfocused high-intensity femtosecond laser pulses," J. Opt. Soc. Am. B **14**(3), 650–660 (1997).

45. J.-F. Ripoche, G. Grillon, B. Prade, M. Franco, E. Nibbering, R. Lange, and A. Mysyrowicz, "Determination of the time dependence of n$_2$ in air," Opt. Commun. **135**(4-6), 310–314 (1997).

46. S. A. Mousavi, H. C. H. Mulvad, N. V. Wheeler, P. Horak, J. Hayes, Y. Chen, T. D. Bradley, S.-U. Alam, S. R. Sandoghchi, E. N. Fokoua, D. J. Richardson, and F. Poletti, "Nonlinear dynamic of picosecond pulse propagation in atmospheric air-filled hollow core fibers," Opt. Express **26**(7), 8866–8882 (2018).

47. L. C. Van, A. Anuszkiewicz, A. Ramaniuk, R. Kasztelanic, K. D. Xuan, V. C. Long, M. Trippenbach, and R. Buczyński, "Supercontinuum generation in photonic crystal fibers in core filled with toluene," J. Opt. **19**(12), 125604 (2017).

48. L. C. Van, V. T. Hoang, V. C. Long, K. Borzycki, K. D. Xuan, V. T. Quoc, M. Trippenbach, R. Buczyński, and J. Pniewski, "Supercontinuum generation in photonic crystal fibers infiltrated with nitrobenzene," Laser Phys. **30**(3), 035105 (2020).

49. P. Zhao, M. Reichert, S. Benis, D. J. Hagan, and E. W. V. Stryland, "Temporal and polarization dependence of the nonlinear optical response of solvents," Optica **5**(5), 583–594 (2018).

50. L. Liu, T. Cheng, K. Nagasaka, H. Tong, G. Qin, T. Suzuki, and Y. Ohishi, "Coherent mid-infrared supercontinuum generation in all-solid chalcogenide microstructured fibers with all-normal dispersion," Opt. Lett. **41**(2), 392–395 (2016).

51. Y. Li, L. Wang, M. Liao, Y. Liu, X. Li, W. Bi, F. Yu, L. Zhang, Y. Jiang, Z. Wang, L. Zhang, C. Yuan, and L. Hu, "Step-index fluoride fibers with all-normal dispersion for coherent mid-infrared supercontinuum generation," J. Opt. Soc. Am. B **36**(11), 2972–2980 (2019).

52. M. Diouf, A. B. Salem, R. Cherif, H. Saghaei, and A. Wague, "Super-flat coherent supercontinuum source in As$_{38.8}$Se$_{61.2}$ chalcogenide photonic crystal fiber with all-normal dispersion engineering at a very low input energy," Appl. Opt. **56**(2), 163–169 (2017).

53. D. Dobrakowski, A. Rampur, G. Steępniewski, A. Anuszkiewicz, J. Lisowska, D. Pysz, R. Kasztelanic, and M. Klimczak, "Development of highly nonlinear polarization-maintaining fibers with normal dispersion across entire transmission window," J. Opt. **21**(1), 015504 (2019).

54. K. Saitoh and M. Koshiba, "Empirical relations for simple design of photonic crystal fibers," Opt. Express **13**(1), 267–274 (2005).

55. M. Koshiba and K. Saitoh, "Applicability of classical optical fiber theories to holey fibers," Opt. Lett. **29**(15), 1739–1741 (2004).

56. T. Miya, Y. Terunuma, T. Hosaka, and T. Miyashita, "Ultimate low-loss single-mode fibre at 1.55 μm," Electron. Lett. **15**(4), 106–108 (1979).

57. R. H. Stolen, J. P. Gordon, W. J. Tomlinson, and H. A. Haus, "Raman response function of silica-core fibers," J. Opt. Soc. Am. B **6**(6), 1159–1166 (1989).

58. P. D. Drummond and J. F. Corney, "Quantum noise in optical fibers. I. Stochastic equations," J. Opt. Soc. Am. B **18**(2), 139–152 (2001).

59. J. M. Dudley and S. Coen, "Coherence properties of supercontinuum spectra generated in photonic crystal and tapered optical fibers," Opt. Lett. **27**(13), 1180–1182 (2002).

60. G. P. Agrawal, *Nonlinear fiber optics* (Academic, 2006), 4th ed.

61. P. D. Maker, R. W. Terhune, and C. M. Savage, "Intensity-dependent changes in the refractive index of liquids," Phys. Rev. Lett. **12**(18), 507–509 (1964).

62. S. Wabnitz, "Modulational polarization instability of light in a nonlinear birefringent dispersive medium," Phys. Rev. A **38**(4), 2018–2021 (1988).
63. J. E. Rothenberg, "Modulational instability for normal dispersion," Phys. Rev. A **42**(1), 682–685 (1990).
64. J. J. Ferreiro, R. de la Fuente, and E. López-Lago, "Characterization of arbitrarily polarized ultrashort laser pulses by cross-phase modulation," Opt. Lett. **26**(13), 1025–1027 (2001).
65. P. Schlup, O. Masihzadeh, L. Xu, R. Trebino, and R. A. Bartels, "Tomographic retrieval of the polarization state of an ultrafast laser pulse," Opt. Lett. **33**(3), 267–269 (2008).
66. L. Xu, P. Schlup, O. Masihzadeh, R. A. Bartels, and R. Trebino, "Analysis of the measurement of polarization-shaped ultrashort laser pulses by tomographic ultrafast retrieval of transverse light E fields," J. Opt. Soc. Am. B **26**(12), 2363–2369 (2009).
67. A. V. Gorbach and D. V. Skryabin, "Soliton self-frequency shift, non-solitonic radiation and self-induced transparency in air-core fibers," Opt. Express **16**(7), 4858–4865 (2008).
68. Y. Yuan, P. Yang, X. Peng, Z. Cao, S. Ding, N. Zhang, Z. Liu, P. Zhang, X. Wang, and S. Dai, "Ultrabroadband and coherent mid-infrared supercontinuum generation in all-normal dispersion Te-based chalcogenide all-solid microstructured fiber," J. Opt. Soc. Am. B **37**(2), 227–232 (2020).
69. C. Brahms, T. Grigorova, F. Belli, and J. C. Travers, "High-energy ultraviolet dispersive-wave emission in compact hollow capillary systems," Opt. Lett. **44**(12), 2990–2993 (2019).
70. A. Zaytsev, C.-H. Lin, Y.-J. You, C.-C. Chung, C.-L. Wang, and C.-L. Pan, "Supercontinuum generation by noise-like pulses transmitted through normally dispersive standard single-mode fibers," Opt. Express **21**(13), 16056–16062 (2013).
71. A. A. Rieznik, A. M. Heidt, P. G. Konig, V. A. Bettachini, and D. F. Grosz, "Optimum Integration Procedures for Supercontinuum Simulation," IEEE Photonics J. **4**(2), 552–560 (2012).
72. J. Hult, "A Fourth-Order Runge-Kutta in the Interaction Picture Method for Simulating Supercontinuum Generation in Optical Fibers," J. Lightwave Technol. **25**(12), 3770–3775 (2007).
73. A. M. Heidt, "Efficient Adaptive Step Size Method for the Simulation of Supercontinuum Generation in Optical Fibers," J. Lightwave Technol. **27**(18), 3984–3991 (2009).
74. R. C. Jones, "A New Calculus for the Treatment of Optical Systems I. Description and Discussion of the Calculus," J. Opt. Soc. Am. **31**(7), 488–493 (1941).
75. J. S. Feehan, F. Ö. Ilday, W. S. Brocklesby, and J. H. V. Price, "Simulations and experiments showing the origin of multiwavelength mode locking in femtosecond, Yb-fiber lasers," J. Opt. Soc. Am. B **33**(8), 1668–1676 (2016).
76. P. Yalamanchili, U. Arshad, Z. Mohammed, P. Garigipati, P. Entschev, B. Kloppenborg, J. Malcolm, and J. Melonakos, "ArrayFire - A high performance software library for parallel computing with an easy-to-use API," AccelerEyes, Atlanta. Retrieved from: https://github.com/arrayfire/arrayfire (2015).
77. M. Frigo and S. G. Johnson, "The design and implementation of FFTW3," Proc. IEEE **93**(2), 216–231 (2005).
78. https://doi.org/10.15129/791fa14e-8aa1-489f-83a3-777b62c77f00.